

Network of sensitive magnetometers for urban studies

T. A. Bowen^{1,2}, E. Zhivun¹, A. Wickenbrock³, V. Dumont¹,
S. D. Bale^{1,2}, C. Pankow⁴, G. Dobler⁵, J. S. Wurtele¹ and D.
Budker^{1,3,6,7}

¹Department of Physics, University of California, Berkeley, California 94720-7300, USA

²Space Sciences Laboratory, University of California, Berkeley, California 94720-7300, USA

³Johannes Gutenberg-Universität Mainz, 55128 Mainz, Germany

⁴Center for Interdisciplinary Exploration & Research in Astrophysics (CIERA),
Northwestern University, Evanston, IL 60208, USA

⁵Center for Urban Science and Progress, New York University, Brooklyn, NY 11201, USA

⁶Helmholtz Institut Mainz, 55128 Mainz, Germany

⁷Lawrence Berkeley National Laboratory, Berkeley, CA 94720

E-mail: tbowen@berkeley.edu

Abstract. The magnetic signature of an urban environment is investigated using a geographically distributed network of fluxgate magnetometers deployed in and around Berkeley, California. The system hardware and software are described and results from initial operation of the network are reported. The sensors sample the vector magnetic field with a 4 kHz resolution and are sensitive to fluctuations below $0.1 \text{ nT}/\sqrt{\text{Hz}}$. Data from separate stations are synchronized to around $\pm 100 \mu\text{s}$ using GPS and computer system clocks. Data from all sensors are automatically uploaded to a central server. Anomalous events, such as lightning strikes, have been observed. A wavelet analysis is used to study observations over a wide range of temporal scales up to daily variations that show strong differences between weekend and weekdays. The Bay Area Rapid Transit (BART) is identified as the most dominant signal from these observations and a superposed epoch analysis is used to study and extract the BART signal. Initial results of the correlation between sensors are also presented.

Keywords: Magnetometry, urban studies. Submitted to: *New J. Phys.*

1. Introduction

Measuring magnetic fields on different spatiotemporal scales can reveal a variety of information about the nature of field sources. High cadence field measurements can be used for magnetic-anomaly detection (MAD), which has numerous security applications, such as naval defense and unexploded ordnance detection [1]. Additionally, geographically distributed magnetometers, operating at high sample rates, have been designed to

study the global distribution of lightning strikes using the Schumann resonance [2].

Low frequency measurements, corresponding to large length scales, provide important information relating to the nature of magnetic sources in the Earth's core, maps of near-surface fields, as well as crustal composition and structure models [3]. An international consortium of magnetometer arrays, known as SuperMag, comprises approximately 300 magnetometers operated by numerous organizations [4, 5]. The magnetic field data collected from these stations is uniformly processed and provided to users in a common coordinate system and timebase [5]. Such data are important to global-positioning-system (GPS)-free navigation, radiation-hazard prediction[‡], climate and weather modeling, and fundamental geophysics research. Additionally, measurements of the auroral magnetic field are necessary in testing models for space-weather prediction, which aims to mediate hazards to satellite communications and GPS from solar storms [6, 7, 8].

Magnetometry has additionally been applied in the search for earthquake precursors. Anomalous enhancements in ultra low frequency (ULF) magnetic fields were reported leading up to the October 17, 1989 Loma Prieta earthquake [9]. Similar anomalous geomagnetic behavior was observed for the month preceding the 1999 Chi-Chi earthquake in Taiwan [10]. Recently, attempts have been made to study precursors to the 2011 Tohoku earthquake in Japan [11].

Despite magnetometry's numerous applications, measurements of magnetic fields frequently suffer from contamination from unrelated, and often unknown, sources. In their search for earthquake precursors, Fraser-Smith et al. (1978) found that magnetic noise from the Bay Area Rapid Transit (BART) system dominated their ULF sensors [12]. This noise is evident in Fig. 1, which depicts the magnitude of the magnetic field recorded at the University of California (UC) Berkeley Botanical Garden. Despite the obvious presence of local permanent or time-varying magnetic contamination, the recorded magnetic field is dominated by fluctuations beyond the expected typical geomagnetic values. These fluctuations diminish dramatically between approximately 1 AM and 5 AM local time, indicating that these are the same fluctuations [12] attributed to the operation of BART.

Even during the magnetically quieter nighttime period, there remain fluctuations which exceed expected geophysical values. Certainly, some of the field variation can be attributed to variations in the ionospheric dynamo and other natural sources: similar trends appear in the magnetic record from the Botanical Garden as well as Intermagnet data from a magnetometer located in the nearby city of Fresno [13][§]. Nevertheless, the contribution of human activity to these nighttime fluctuations remain poorly understood.

[‡] http://www.nws.noaa.gov/os/assessments/pdfs/SWstorms_assessment.pdf

[§] <http://www.intermagnet.org/>

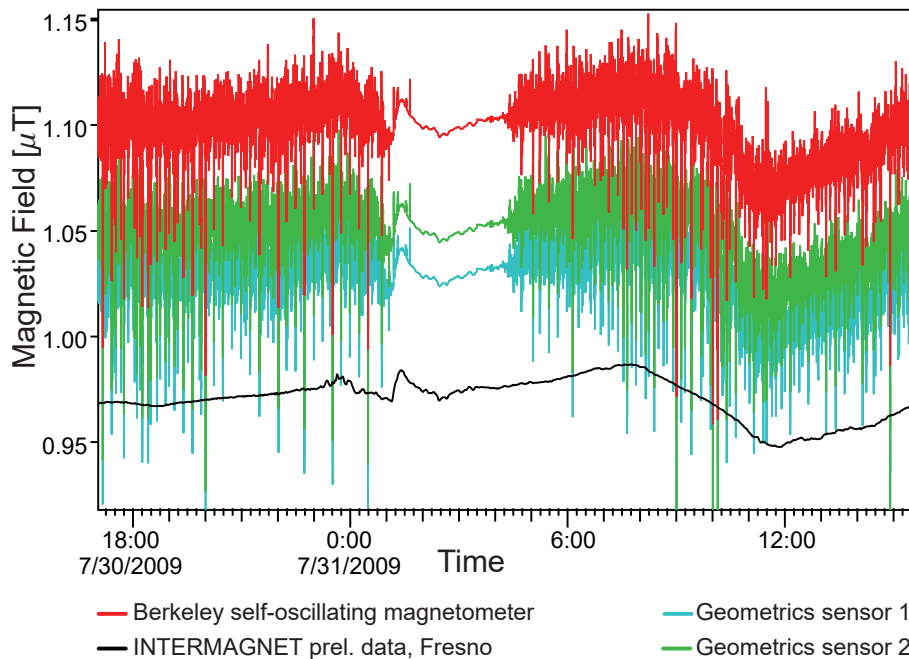


Figure 1. The Earth’s magnetic field, as recorded at the UC Berkeley Botanical Garden. The red trace represents measurements taken by an all-optical self-oscillating magnetometer designed and constructed at UC Berkeley in partnership with Southwest Sciences, Inc. [14]. The green and blue traces are data taken with a commercially available cesium magnetometer from Geometrics, Inc. The gray trace represents the average field seen by a geomagnetic observatory located in Fresno, CA.

This paper reports on the development of a synchronized magnetometer array operating at high-cadence in and around Berkeley, California. The array of four magnetometers seeks to observe the city through its dynamic magnetic signature. This novel technique is part of the wider emerging field of data-intensive science.

Recently, a wide variety of technologies have been applied to observe urban environments. For example, multi-frequency spectral observations of a city have been implemented to classify static properties of built structures [15]. Imaging spectrometers have been employed [16, 17] to differentiate lighting technologies. Visual synoptic measurements from a camera operating at a 10 second cadence have characterized lighting behavior in 4,000 light sources in Manhattan over multiple weeks [18].

In Sec. 2 we briefly describe the components and performance of the hardware and software implemented in magnetometer array. We emphasize our preference for commercially available hardware and advanced timing algorithms and utilize techniques similar to those of the Global Network of Optical Magnetometers for Exotic (GNOME) physics project [19].

The analysis of our data is presented in Sec. 3. In Sec. 3.1 we present the signatures of

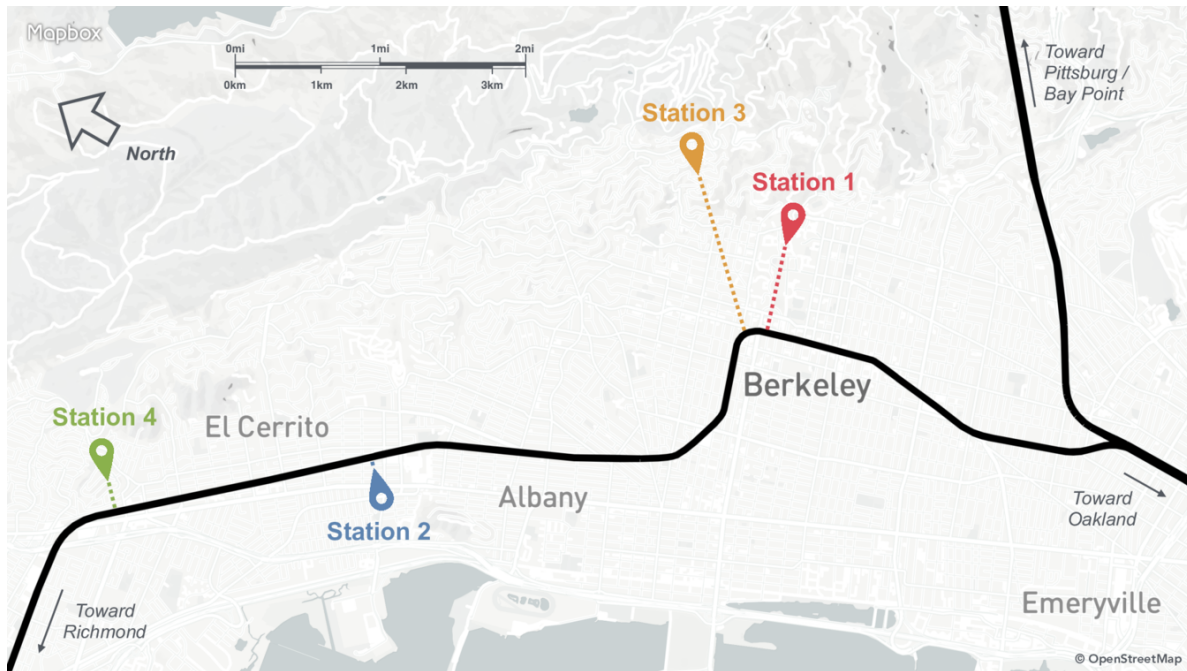


Figure 2. Map of Berkeley and location of the stations. The colored pins identify the locations of the magnetometers in our network. The black line shows the different paths of the BART trains. The shortest distance from each magnetometer station to the nearby BART line is represented by the dashed lines. Stations 1 to 4 are respectively located 1000, 130, 2000 and 360 meters from the closest BART line.

several common urban sources and observe the signature of a lightning strike. Station data is analyzed and compared in Sec. 3.2. Clear variations between weekday and weekend, day and night, and distance from BART tracks are observed. Measurements are examined with wavelets in Sec. 3.3. Initial results of correlating station results are presented. In Sec. 4, we present an initial method to isolate the BART signal. Conclusions and directions for future research are presented in Sec. 5.

2. Instrumentation, Hardware, and Data Acquisition

2.1. Description of the system

Our magnetometer network consists of several spatially separated magnetometers with high precision timing for correlation analysis. Figure 2 shows a map of Berkeley with the sensor locations of the network. High precision timing can be achieved with commercial hardware, such as a real-time data acquisition system disciplined to an external time source^{||}. Our approach to system design is to utilize consumer components wherever possible. Each station consists of a general-purpose laptop computer with an inexpensive GPS receiver. The penalty for avoiding bulky and expensive hardware, which increases costs and reduces mobility, was to write custom high-precision timing software. This

^{||} <http://sine.ni.com/nips/cds/view/p/lang/en/nid/209847/>

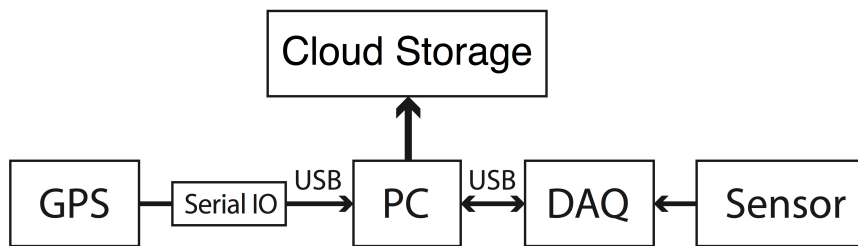


Figure 3. A schematic of a magnetometer station. The computer (PC) retrieves the magnetic field vector value continuously from the data acquisition system (DAQ) that reads out the voltage on the sensor. The timing data are provided by a global-positioning-system GPS receiver, with a dedicated 1 pulse-per-second (PPS) output through a Serial IO RS232-to-USB converter. The acquired data are uploaded to a shared Google Drive folder.

approach reduces the cost of the acquisition system by an order of magnitude, allows for portable sensors, and enables battery operation.

A schematic of a single magnetometer is presented in Fig. 3. Each setup is controlled by a computer (PC, ASUS X200M) running Windows 10 operating system (OS). The PC acquires magnetic field data from the DAQ (Biomed eMains Universal Serial Bus, USB, 24 bit) and timing data from the GPS receiver (Garmin 18x LVC). The DAQ continuously samples the fluxgate magnetometer (MAG, Biomed eFM3A) at a rate of 3960 sample/s. Absolute timing data are provided once per second by the GPS receiver, which is connected through a powered high-speed RS232-to-USB converter (SIO-U232-59). The GPS pulse-per-second signal, with $1\ \mu\text{s}$ accuracy, is routed to the computer through the carrier detect (CD) pin of the RS232 converter. Data from the DAQ arrive in packets of 138 vector samples approximately every 35 ms. As the data are received, they are recorded together with the GPS information and the computer system clock. Data are uploaded via wireless internet to a shared Google Drive folder.

2.2. Time synchronization and filtering

Time intervals between the GPS updates are measured by the computer system clock (performance counter), which runs at 2533200 Hz. A linear fit model is used to determine the absolute system time relative to the GPS. Only the GPS timing data from the last 120 seconds are used to determine the linear fit parameters. When the magnetic-field data packet is received, the performance counter value is recorded immediately. The packet time-tag is determined from interpolating the linear fit GPS time to the performance counter value. Typical jitter of the inferred time stamps is $120\ \mu\text{s}$ and is limited by the USB latency [20].

Some of the data packets cannot be processed immediately due to OS limitations. These packets are delayed by up to several milliseconds before being delivered to the data-acquisition software. The number of the delayed packets depends on the system load.

During normal operation of a magnetometer, the average fraction of the delayed packets is about 3%. The intervals between both GPS and packet arrival times are measured with the performance counter in order to identify the delayed packets. Any GPS data that arrive more than $50 \mu\text{s}$ late are discarded from the linear-fit model. When the magnetometer data arrive with a $200 \mu\text{s}$ or greater discrepancy from the expected time, their time stamp is replaced with the expected arrival time, which is inferred from the linear fit. Our time filtering algorithm and data acquisition software are publicly available on GitHub[¶].

2.3. Performance characterization

In order to characterize the performance of the data acquisition system, we apply a reference signal simultaneously to the sensors. The sensors are placed into a Helmholtz coil system driven by a pulse generator. The amplitude of the pulses is $2 \mu\text{T}$, the period is 200 ms, and the duty cycle is 50% (Fig. 4a). The top and bottom rows in Fig. 4 represent the data before and after application of the timing correction algorithm. The inset in Fig. 4a demonstrates how a delay in retrieving a data packet disrupts the timing of the field pulses. When a data packet is delayed, the magnetic field samples are distributed over a slightly larger time period, which affects the estimated time of the field change. In Fig. 4 interpolated time of the falling edge from sensor four has been several milliseconds after the field changed, causing the zero crossing of the square wave to shift in time from the other sensors. Fig. 4b shows the time discrepancies between the interpolated and expected square wave zero crossings. The zero crossings are recorded with $120 \mu\text{s}$ standard deviation from the expected interval; however, there are a large number of outliers with up to a 10 ms discrepancy. Figure 4c shows the histogram of the data from 4b, where the red curve represents the best fit Gaussian. After the timing correction algorithm is applied to the data, time stamps associated with outlier packets are replaced with the expected arrival times (Fig. 4 d,e,f). The remaining jitter is a Gaussian distributed with an error of $120 \mu\text{s}$.

2.4. Instrumental noise floor

Figure 5 shows the instrumental noise floors for each vector axis of a Biomed magnetometer. Data were obtained in a two layer μ -metal shield can for approximately 35 minutes (2^{23} samples at 3960 sample/s). Power spectral densities were calculated over 2^6 (64) chunks of 2^{17} sample intervals; the noise floor is taken as the average of the power spectra ensemble. The noise floor varies between individual axes, with the most noise observed on the Z-axis. For all three directions, the noise floor is constant between $\approx 2 \text{ Hz}$ and $\approx 700 \text{ Hz}$. Narrowband spectral noise from 60 Hz and harmonics is easily observed in the data. For frequencies above 1 Hz, the noise floor is uniformly below $0.1 \text{ nT}/\sqrt{\text{Hz}}$.

¶ <https://github.com/lenazh/UrbanMagnetometer>

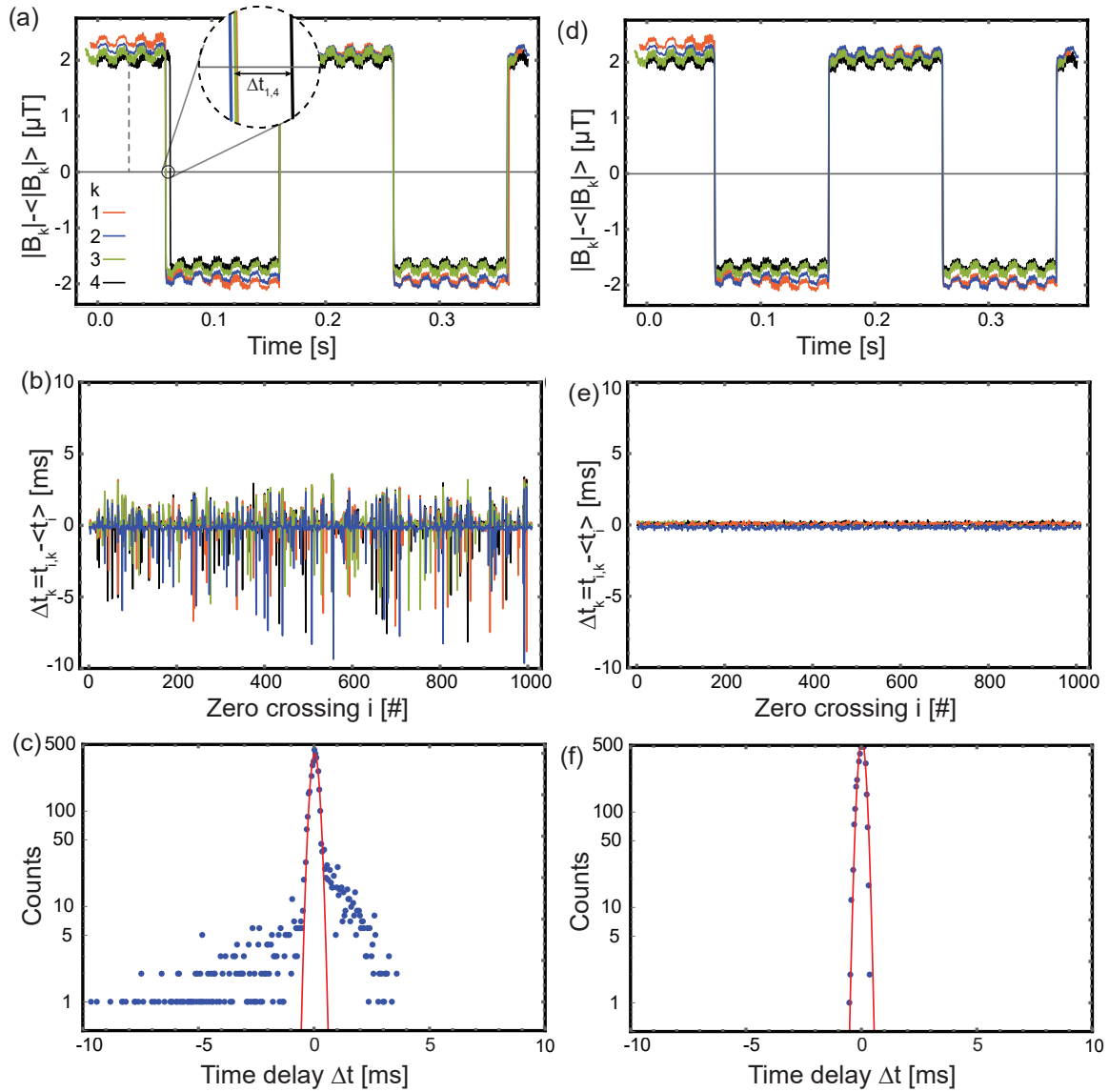


Figure 4. Characterization measurement of the time synchronization algorithm. The four magnetometers are subjected to the same square-wave-modulated magnetic field. The top row shows the measurement with the unprocessed time information. The bottom row shows the same data with the corrected time. (a) Time series of the four magnetometer traces. The inset shows a time discrepancy of magnetometer 4 at the zero crossing. (b) The difference of the mean zero crossing time of the square wave and the individual zero-crossing time for each magnetometer for two minutes of data. The data show a spread and delays of up to 10 ms. (c) histogram of the data in (b), with the red curve representing the best-fit Gaussian. While most zero-crossing events have the correct timing within $120 \mu\text{s}$ (standard deviation of the Gaussian), there are a significant number of outliers. (d), (e) and (f) show the same data after implementing the time synchronization algorithm.

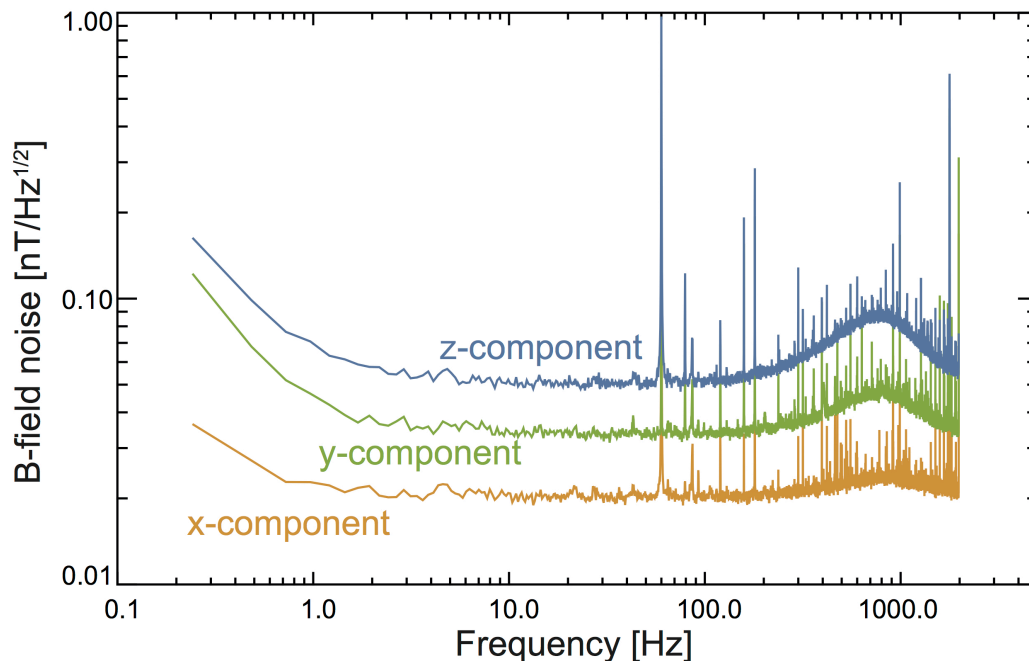


Figure 5. Instrumental noise floors for each vector axis of a Biomed magnetometer.

3. Data Analysis

3.1. Observations of urban magnetic signatures

The portability of our sensors have enabled the direct measurement of several urban field sources. Figure 6 shows the magnetic signatures of several field sources associated with transportation: traffic on a freeway, as well as both Amtrak and BART trains. Figure 7, shows a spike in the magnetic field due to a lightning strike recorded by three geographically distributed sensors. This lightning strike, which occurred before implementation of the timing correction algorithm, highlights the need for time-corrected data: without the timing algorithm, the sensors' clocks can drift, in this case up to ≈ 50 ms. This 50 ms discrepancy corresponds to an unreasonable spatial separation of 15,000 km. Unfortunately, no further lightning strikes have been captured since implementation of the timing algorithm: the synchronous occurrence of lightning in our network will eventually provide an important test of our timing algorithm. We only use data from Stations 2, 3 and 4 in multi-station comparisons. Station 1 served mainly as an engineering unit for characterisation measurements and other testing.

3.2. Multi-station analysis of magnetic field data

Fraser-Smith et al. (1978) report the presence of strong ultra-low frequency (ULF) magnetic fluctuations throughout the San Francisco Bay Area in the 0.022 to 5 Hz range [12]. The dependence of these fluctuations on proximity to the Bay Area Rapid Transit (BART) lines, and their correspondence with train time tables, led the authors to

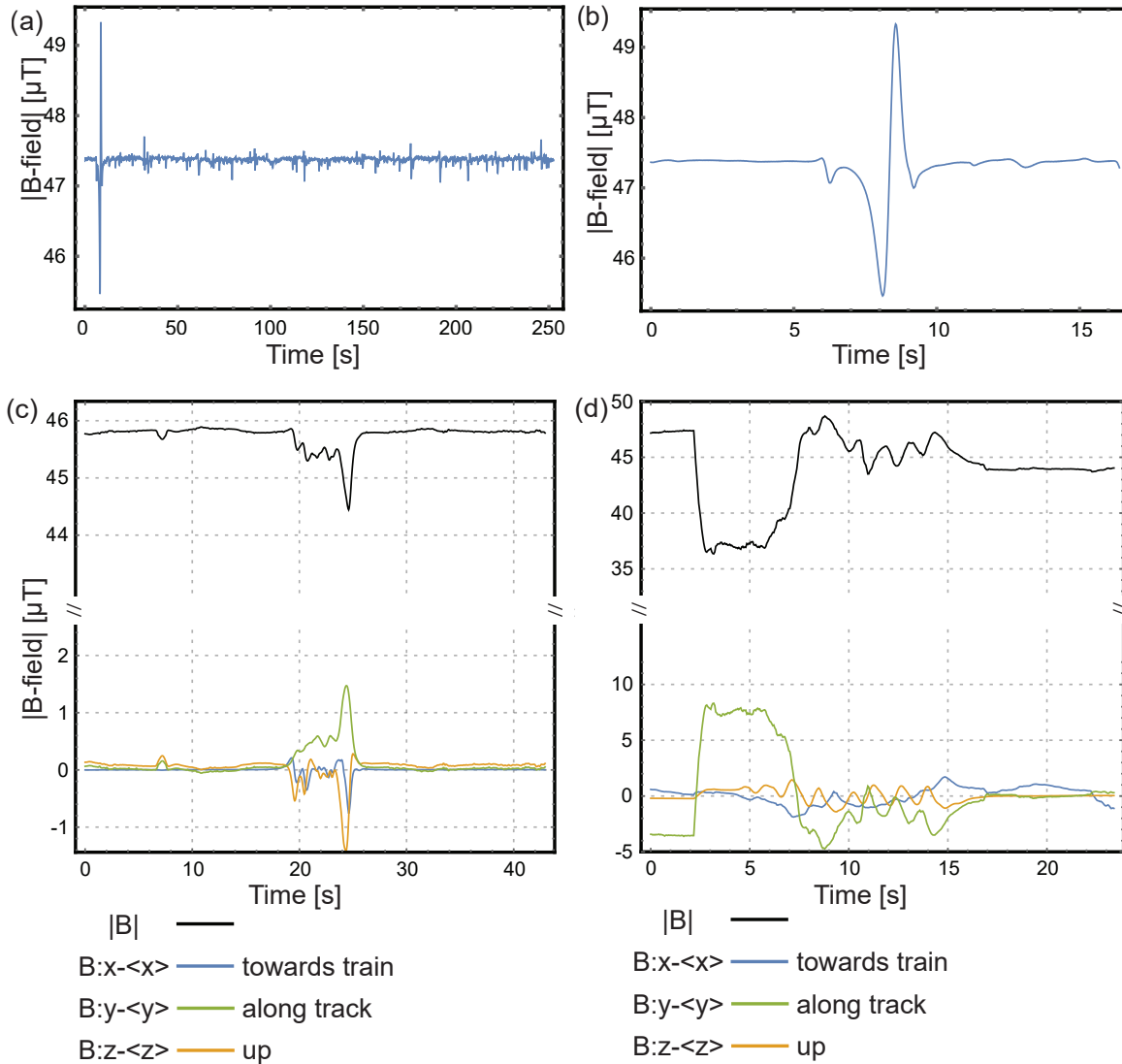


Figure 6. Examples of urban magnetic sources. (a) Scalar magnitude field measurements from sensor placed 5m from highway. (b) Signature of large truck passing on highway (first peak in (a)). (c) Magnetometer placed close to the tracks of a passing Amtrak train. The scalar magnitude field is shown in black with the vector components (DC removed) displayed in color. (d) Data taken at El Cerrito BART station of a Fremont (south) bound train.

attribute this ULF signal to currents in the BART rail system. The location of our network stations, as well as our high timing accuracy and length of recorded intervals, ensures that urban signatures, such as BART, will be present in our data.

The timing algorithm provides sub-microsecond resolution for MAD; however many magnetic signatures related to anthropogenic activity occur at low frequencies where GPS alone provides adequate timing. To investigate urban magnetic fluctuations, we decimate the full 3,960 sample/s to a 1 sample/s cadence. Antialiasing is accomplished with a moving average (boxcar) filter. Low-cadence data provide adequate resolution for

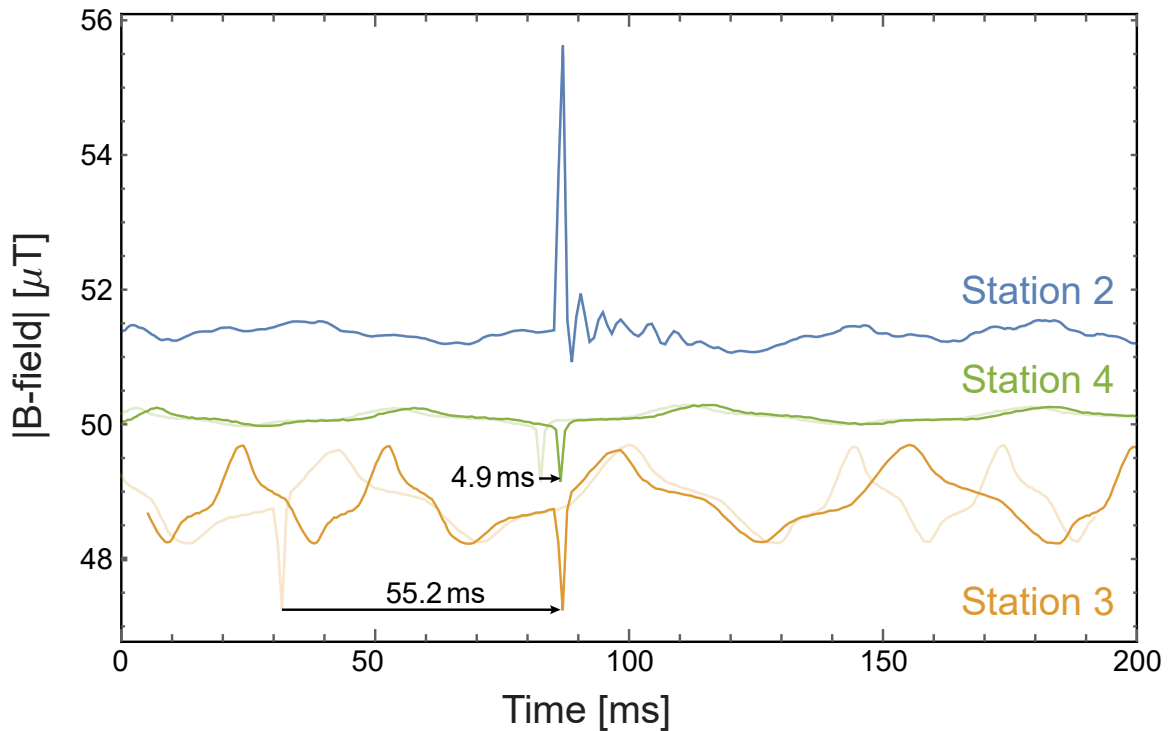


Figure 7. Magnetic anomaly detection. Observations from three geographically distributed magnetometers of a single lightning strike. At the time of the strike, the timing issues described in Section 2.2 had not been resolved. Magnetometer traces from each station were shifted to align the spikes, demonstrating the need for a precision timing algorithm. Looking at the apparent frequency change in the 60 Hz power-line signature of the yellow trace, we infer that timing errors occurred in this sensor just before the lightning strike. The blue trace was shifted up by $2 \mu\text{T}$ for plotting purposes. Station 1 served as an engineering unit and was not part of the ongoing observations.

correlating multi-station observations, while simultaneously removing the 60 Hz power signal.

Figure 8 shows the scalar magnitude fluctuations of three stations on Sunday, 03/20/2016 (PDT). One-day scalar average magnitudes are subtracted from the total magnitude. Each panel additionally shows geomagnetic field data (1 minute averaged) acquired from the United States Geological Survey (USGS) station in Fresno, CA. Though panel (a) demonstrates a general agreement between our record and the USGS data, consistent large fluctuations in excess of the geomagnetic field are observed in each sensor. Panel (b) shows that these non-geomagnetic fluctuations dominate the daytime magnetic field. Additionally, panel (c) shows a subset of the data from 10-11 AM, revealing several synchronous spikes in each sensor.

A magnetically quiet period corresponding to BART operating hours⁺ is evident in

⁺ <https://www.bart.gov/>

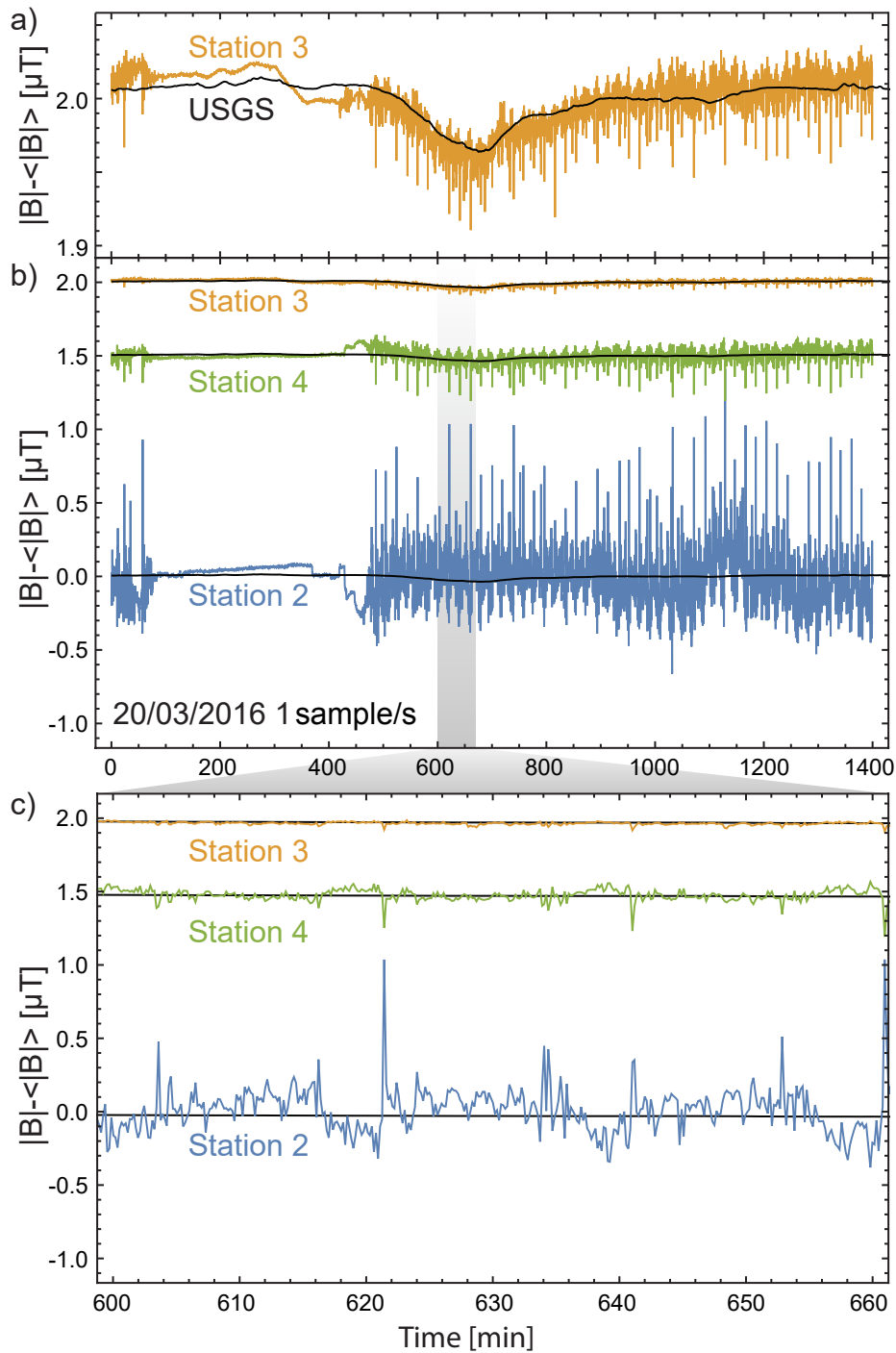


Figure 8. Magnetic field magnitudes for three stations at 1 sample/s cadence on 03-20-2016. Panel (a) shows close agreement between the USGS station in Fresno and sensor 3, demonstrating our stations sensitivity to geomagnetic fields. Panel (b) shows the 24 hour scalar magnitudes (DC values were adjusted for plotting purposes) for all three active sensors; the magnitude of fluctuations corresponds with the distance from each sensor to the BART train line. The bottom panel (c) shows one hour of data from 10-11 AM (PDT). The 24 hour scalar field averages have been removed from each time-series. The one minute averaged USGS geomagnetic field data are shown in each plot.

the records of the three active sensors (stations 2-4). Figure 9 shows the distribution of magnitude fluctuations binned at 10^{-3} nT. Separating the records into two intervals - defined by the arrival of the last evening and departure of the first morning trains (1:26AM - 7:55 AM) - reveals characteristically different distribution functions corresponding to the night (no BART) and day (active BART) magnetic records. For each sensor, the nighttime distribution functions appear as a superposition of several individual peaks. Standard deviations, σ_i , for the nighttime distribution functions of the three active sensors are given by $\sigma_2 = 0.072 \mu\text{T}$, $\sigma_3 = 0.009 \mu\text{T}$, and $\sigma_4 = 0.026 \mu\text{T}$.

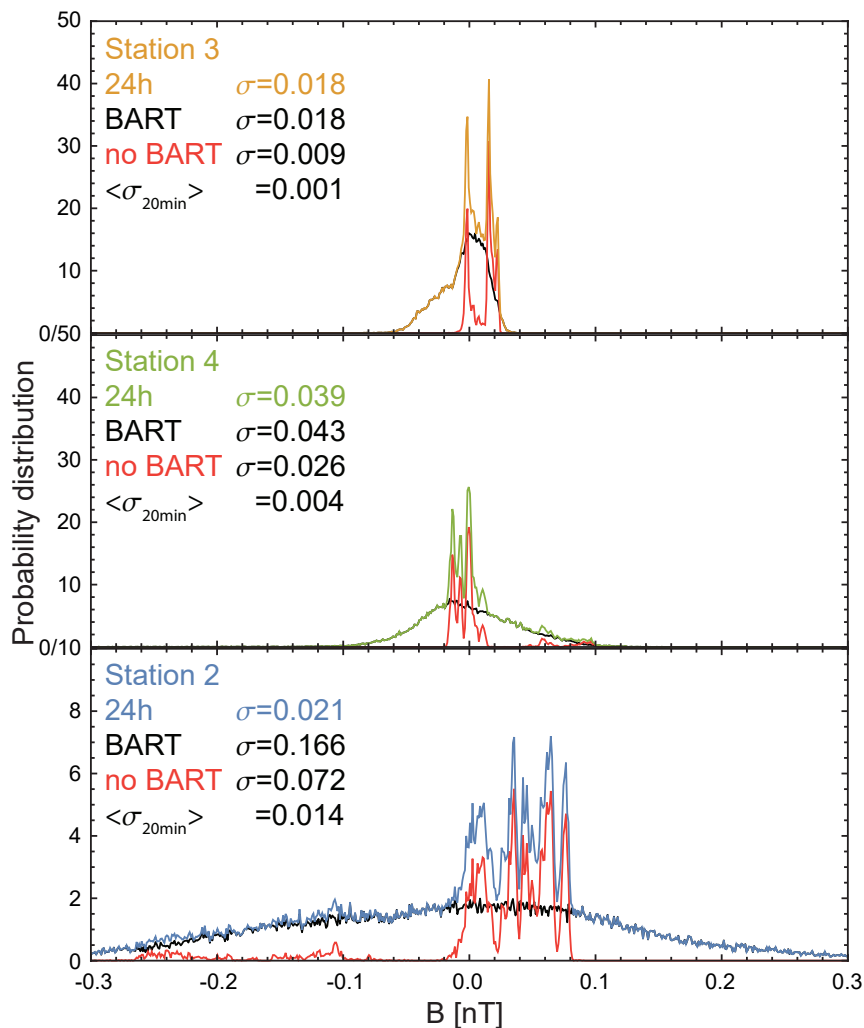


Figure 9. Distributions for 24hr, daytime, and nighttime magnetic field observations. The nighttime observations show several discrete peaks, daytime fluctuations follow broad distributions. The variance of the distributions corresponds with geographic distance from the Fremont/Richmond BART line.

Figure 10 shows that the time-localized variance of magnetic field fluctuations, calculated in a 40 minute sliding-window, is significantly smaller than the variance calculated

for the full nighttime interval. This indicates that the discrete peaks observed in the nighttime distribution functions are localized in time, while transitions in the DC field magnitude cause the appearance of several distinct peaks. These transitions in the DC field are evident as peaks in the sliding-window variance. The simultaneous occurrence of transitions in the DC field magnitude, evidenced by simultaneous peaks in the sliding window variance, suggests that these transitions are global phenomena, perhaps relating to nighttime maintenance on the BART line or activity in the ionosphere.

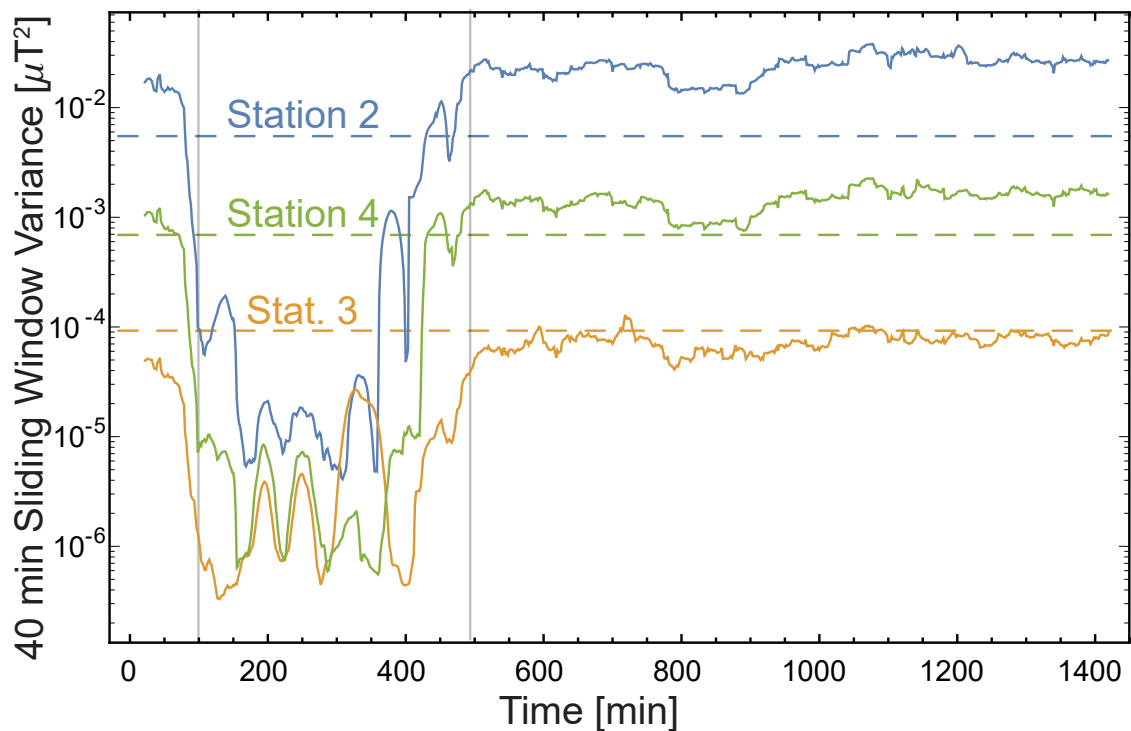


Figure 10. Magnetic field variance calculated over 40-minute sliding window for all three sensors. Vertical lines mark the night interval when BART is inactive. Strong, discontinuous, transitions in the DC field amplitude, observed as peaks in the sliding window variance, cause the variance calculated over the entire night interval to be significantly larger than the time-local variance.

The two vertical bars in Fig. 10 mark the period for which BART is inactive. Increased field variance, i.e. signal power, is clearly tied to the operation of BART. Figure 10 also highlights the relatively constant daytime variance in each station. Additionally, there appear to be approximately constant ratios between the daytime variance (power) observed by each sensor. This suggests that the background noise level observed in each station is set by the distance to BART. Other anthropogenically generated fields (for example traffic) are most certainly obscured by the large BART signal. Accordingly, identification of further urban signals requires a thorough characterization of the magnetic background generated by BART.

3.3. Time-Frequency (Wavelet) Analysis

Frequency-domain analysis is typically used to reveal the spectral composition of a magnetic time series. Localizing the distribution of spectral power in time requires simultaneous analysis in both time and frequency domains. We implement a continuous wavelet transform (CWT), using Morlet wavelets [21], to investigate the time-frequency distribution of low-frequency fluctuations associated with BART. The unnormalized Morlet wavelet function $\psi(\tau)$ is a Gaussian modulated complex exponential,

$$\psi(\tau) = \pi^{1/4} e^{i\omega_0\tau} e^{-\frac{\tau^2}{2}}, \quad (1)$$

with non-dimensional time and frequency parameters τ and ω_0 . A value of $\omega_0 = 6$ meets the admissibility conditions prescribed in Ref. [22] and is commonly used across disciplines [23, 21]. At each time step, the CWT of the magnetic field B is defined by the convolution of the time series record with a set of scaled wavelets,

$$W(s, t) = \sum_{i=0}^{N-1} B_x(t_i) \psi\left(\frac{t_i - t}{s}\right), \quad (2)$$

which are normalized to maintain unit energy at each scale. The CWT provides a scale independent analysis of time-localized signals, and is additionally insensitive to time series with variable averages (non-stationary signals). These qualities provide some advantage over alternative time-frequency analysis techniques, such as the windowed Fourier transform, which calculates the spectral power density in a sliding window applied to the time series. Introducing a window imposes a preferred scale which can complicate analysis of a signal's spectral composition. For example, low frequencies components, with periods longer than the sliding window scale, are aliased into the range of frequencies allowed by the window, thereby degrading the estimate of spectral density.

Full day, 1 sample/s cadence, wavelet power spectral densities $|W(s, t)|^2$ ($\mu\text{T}^2/\text{Hz}$) for stations 3 and 4 on Sunday, 03/20/2016 (PST) are displayed in Fig. 11. These spectrograms prominently display the quiet nighttime period. Additionally, strong power is observed in several scales corresponding to a fundamental 20 minute period (8.33×10^{-4} Hz) and associated higher harmonics. This 20 minute period coincides with the Sunday BART timetable on the geographically closest BART line (Richmond-Fremont). The black lines display region where boundary effects are likely—this region, known as the cone of influence (COI), corresponding to the e -folding time for the wavelet response to an impulse function.

A brick-wall bandpass filter (i.e. unity gain in the passband, full attenuation in the stop band) is applied to each sensor in the frequency domain between 7×10^{-4} and 1×10^{-2} Hz in order to isolate the bands of power observed in the wavelet power spectra. The top panel of Fig. 12 shows the bandpassed time series for 10-11 AM on

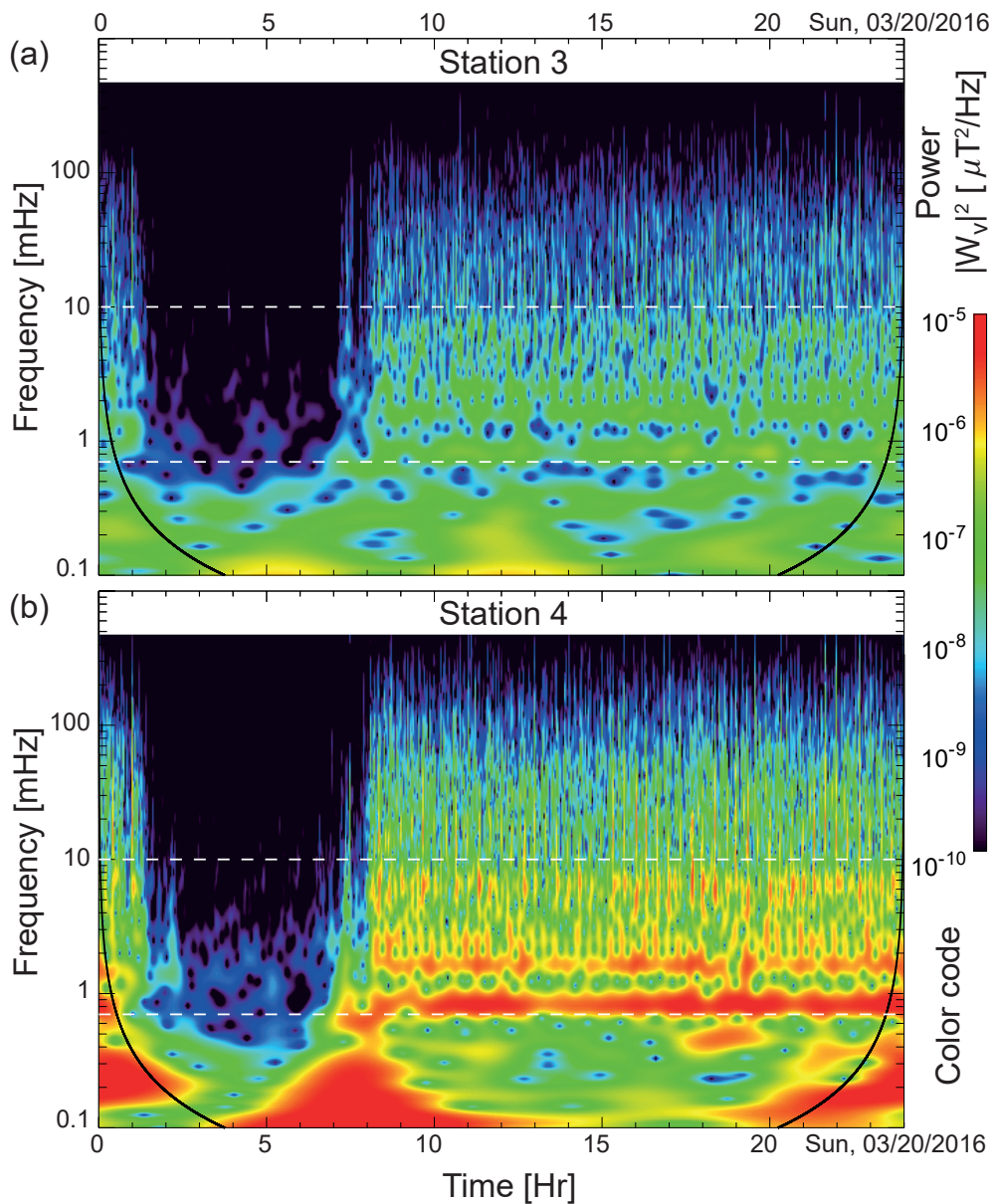


Figure 11. Time-frequency analysis of scalar magnitude magnetometer data. Continuous wavelet transform power spectral densities ($\mu\text{T}^2/\text{Hz}$) for Magnetometer 3 (a) and Magnetometer 4 (b). The spectrograms reveal power in several bands from 8.3×10^{-4} and 1×10^{-2} Hz common to both sensors. These frequencies correspond to a 20 minute period signal and subsequent harmonics. White dashed lines show the frequency range of a brick-wall filter applied to data.

3/20/2016. The bandpassed time series are normalized to their maximum values for the purpose of visualization. This plot immediately suggests that stations 3 and 4 are highly correlated, while station 2 is anti-correlated with stations 3 and 4. Indeed, this is verified by the bottom panel of Fig. 12, which shows the cross correlation coefficients

$C_{ij}(\tau)$ calculated for the 24 hour time series:

$$C_{ij}(\tau) = \frac{\sum_{n=0}^{N-\tau-1} (B_i[n+\tau] - \bar{B}_i)(B_j[n] - \bar{B}_j)}{\sqrt{\left[\sum_{n=0}^{N-1} (B_i[n] - \bar{B}_i)^2 \right] \left[\sum_{n=0}^{N-1} (B_j[n] - \bar{B}_j)^2 \right]}}, \quad (3)$$

where N is the record length, τ is a translation between time series, and n is the sample index [24]. It is clear that stations 3 and 4 are in phase, while station 2 is out of phase of the other two instruments. Interestingly, these phase relationships correspond with the geographical location of the sensors on the east/west side of the BART line (stations 3 and 4 are located east of the rails, while station 2 is located to the west, c.f. Fig. 2).

Figure 13 shows full day wavelet spectral densities for station 2 on both Tuesday, 03/16/2016 and Sunday, 03/20/2016. The quiet BART night is much shorter on Tuesday; this corresponds with the different weekend and weekday time tables. Additionally, Fig. 13 demonstrates the absence of strong power localized to the 20 minute period in the Tuesday data. The weekday timetable is more variable than the Sunday train time table, and it is not possible to clearly identify the BART signal by eye in this case; our future work will explore the correlations between stations and train times in order to fully extract the BART signal.

4. Extracting the BART signal

The periodic signature observed in the Sunday 03/20/2016 time-series can be extracted using the technique known as superposed epoch analysis [25]. Using the time-series generated by station 2, we identified 45 sharp peaks in the magnetic field occurring with an approximately 20 minute period (e.g. Fig. 8). From these 45 peaks, we constructed an ensemble $[X(t)_i]$ of intervals comprising the 3 minutes preceding and 17 minutes succeeding each individual peak. Averaging over the ensemble of intervals $\bar{X}(t) = \sum_i X_i(t)$ reveals a coherent signature with an approximate 20 minute period, Fig. 14(a). The periodic signal observed in the data has the form of a sharp discrete peak of ≈ 1 nT, followed by an oscillation with a period on order of several minutes. Figure 14(b) compares the extracted average signal with an hour of observations taken from 9-10 AM (PDT). The extracted signal provides good qualitative correlation with the hour of observed data. A quantitative comparison is obtained through computing the Pearson correlation

$$\rho_i = \frac{\text{cov}(X_i, \bar{X})}{\sigma_{X_i} \sigma_{\bar{X}}} \quad (4)$$

of the extracted signal with each interval in the ensemble. On average, the correlation between the extracted signal and observed data has a correlation of $\bar{\rho} = 0.74$, with ρ_i ranging from 0.47-0.85. We can interpret these values as the fraction of power in each interval derived from the average signature. In future work, we look to correlate these average signatures between stations and extract the average BART behavior.

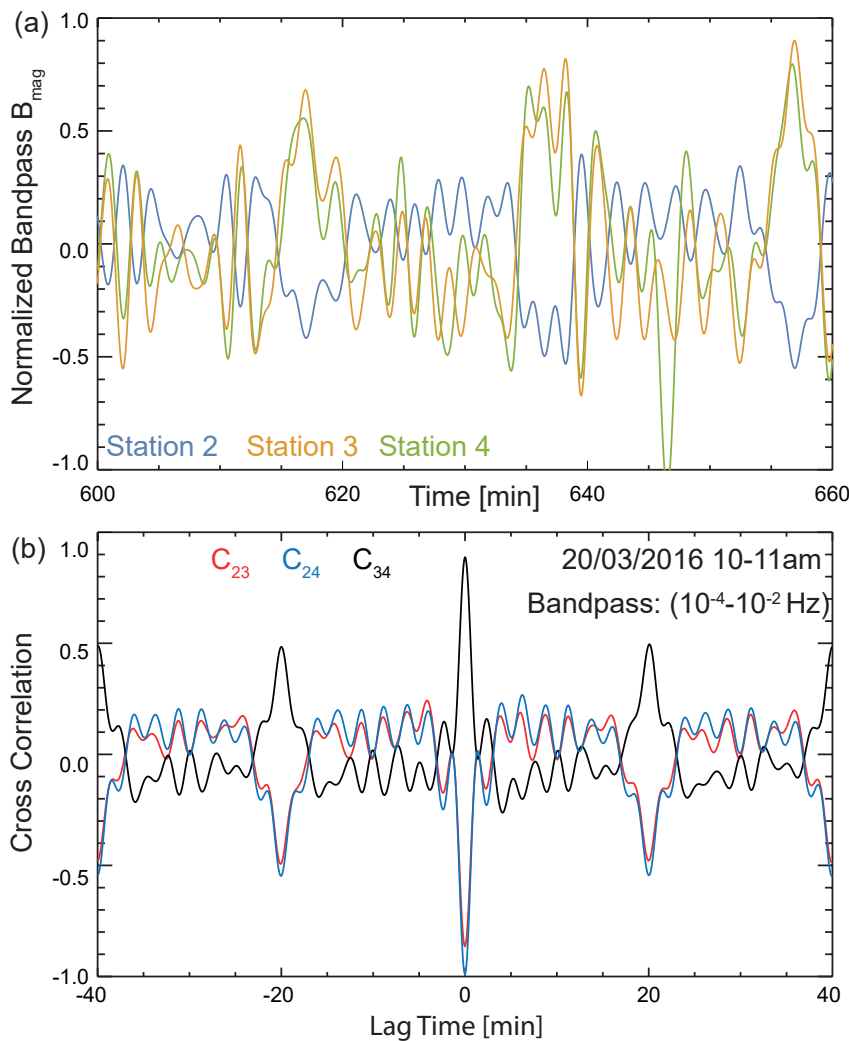


Figure 12. (a) Brickwall bandpassed (7×10^{-4} to 1×10^{-2} Hz) time-series for all three sensors on 03-20-2016 between 10-11 AM (PDT). The bottom panel shows the correlation coefficients between pairs of sensors as a function of lag. Sensors 3 and 4 are highly correlated (in phase), while sensor 2 is anti-correlated (out of phase) with the others. There is a 20 minute periodicity to the data, consistent with the power-bands observed in the wavelet spectra. This 20 minute signal coincides with the published Sunday/Holiday BART schedule for the Fremont/Richmond train line.

5. Discussion

An array of four magnetometers has been developed with bandwidth of DC-kHz and sensitivity better than $0.1 \text{ nT}/\sqrt{\text{Hz}}$. The array is currently deployed in the area surrounding Berkeley, CA, providing measurements of an urban magnetic field. This array is sensitive to both natural magnetic activity, such as lightning and the low frequency variations in the Earth's geomagnetic field, as well as a variety of anthropogenic sources: currents associated with BART, traffic, 60 Hz powerlines. The operation of BART dominates the urban magnetic field generated broadband noise, as well as co-

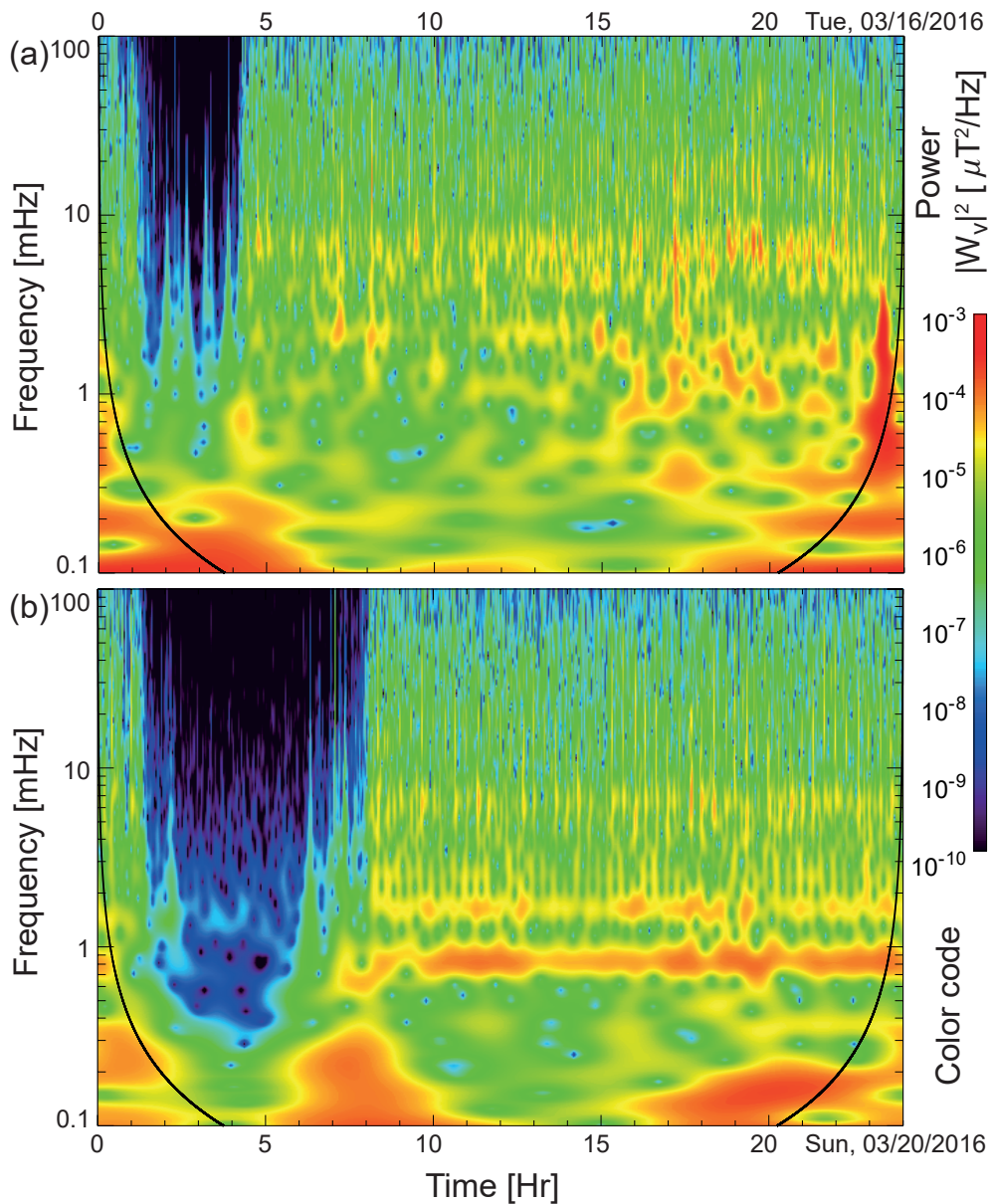


Figure 13. BART night signatures. (a) Continuous wavelet transform of 1 sample/s magnetic field magnitude data from Station 2 on 3/16/2016 (and 3/20/2016). The nighttime signature is significantly shorter in the data taken on Tuesday, this corresponds with BART operating hours. Additionally, the strong power-bands observed on Sunday are not present in the Tuesday data.

herent narrowband spectral features. Significant variation is observed between weekend and weekday magnetic fields, corresponding to variations in the BART train schedule. During the hours in which BART is non-operational, the anthropogenically generated fields are significantly decreased and agreement with the USGS magnetic field measurements is observed. However, the nighttime field still contains a number of features not attributable to geophysical activity. Further study is required to determine the nature and sources of these features. Future work aims to analyze the correlations of the BART

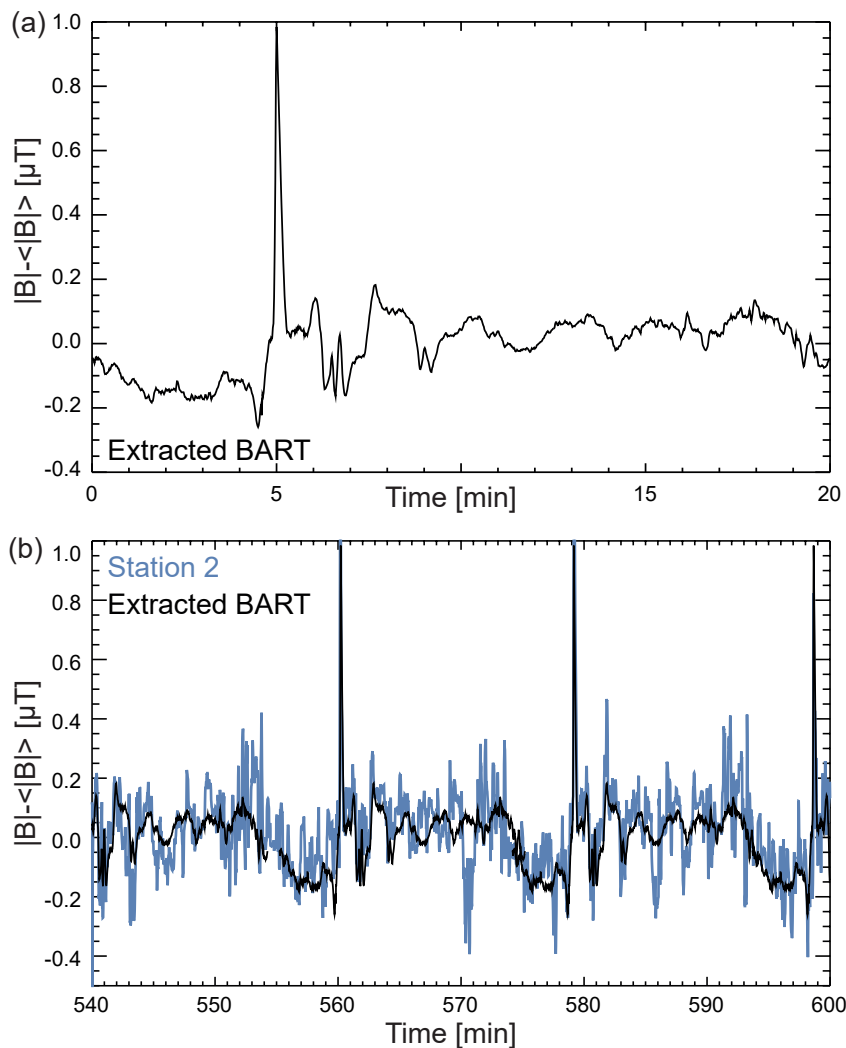


Figure 14. Extraction of BART signal. (a) 20-minute periodic signal of the BART extracted from magnetic field data. (b) Comparison of the extracted average signal with an hour of observations from station 2 taken from 9-10 AM (PDT).

signature between stations and determine the periodic structures associated with the train schedule.

Cross correlating the sensors at high frequencies requires a high-precision timing algorithm to combine the absolute time, acquired through GPS, with the high-precision computer performance clock, local to each station. This algorithm additionally corrects for latency issues associated with the USB interface between the data-acquisition hardware and the system operating system. This timing algorithm has been tested using magnetic fields generated by Helmholtz coils. We intend to use the impulsive globally observable fields generated by lightning to further test our timing algorithm. Our high precision timing will allow for such magnetic anomaly detection on the order of $\approx 100 \mu\text{s}$.

This paper presented a proof-of-concept deployment of what, to our knowledge, is the first synchronized network of magnetometers specifically designed for observing the effects of human activity on the magnetic field in an urban environment. Numerous potential applications and directions for future work have emerged. Further development of algorithms to remove the BART (or any other dominant signal whose source has been identified) must be developed. These algorithms may need to take advantage of other data sources (e.g, the realtime BART schedule) and machine learning techniques. The study of high frequency response (60 Hz and above) has not yet been pursued. We note that anthropogenic fields mask geophysical field fluctuations, and that study of the latter is facilitated by understanding of anthropogenic noise. The magnetic fields due to humans may reflect identifiable aspects of urban dynamics (beyond BART) and these may have correlations other measures of urban life (energy consumption being one of the first to consider). Studies of magnetic field correlations and anomalies may be used to identify and study local phenomena (traffic, elevators, etc.). One spin-off of this research may be improved identification and reduction of anthropogenic noise in geomagnetic measurements located in or near urban environments. The ultimate utility of the magnetometer array as an observational platform for urban systems will only become clear with further studies.

6. Acknowledgements

We are grateful to Brian Patton for his contributions in the early stages of the project. The views expressed in the publication are the author's and do not imply endorsement by the Department of Defense or the National Geospatial-Intelligence Agency.

References

- [1] Sheinker A, Frumkis L, Ginzburg B, Salomonski N and Kaplan B Z 2009 *IEEE Transactions on Magnetism* **45** 160–167 ISSN 0018-9464
- [2] Schlegel K and Füllekrug M 2002 *Physik in unserer Zeit* **33** 256
- [3] Egbert G D 1997 *Geophysical Journal International* **130** 475–496
- [4] Gjerloev J W 2009 *Eos, Transactions American Geophysical Union* **90** 230–231 ISSN 2324-9250 URL <http://dx.doi.org/10.1029/2009E0270002>
- [5] Gjerloev J W 2012 *Journal of Geophysical Research: Space Physics* **117** n/a–n/a ISSN 2156-2202 a09213 URL <http://dx.doi.org/10.1029/2012JA017683>
- [6] Angelopoulos V 2008 *Space Sci Rev* **141** URL <http://dx.doi.org/10.1007/s11214-008-9336-1>
- [7] Peticolas L M, Craig N, Odenwald S F, Walker A, Russell C T and Angelopoulos V 2008 *Space Sci. Rev* **141** URL <http://dx.doi.org/10.1007/s11214-008-9458-5>
- [8] Harris S E, Mende S B, Angelopoulos V, Rachelson W, Donovan E and Jackel B 2008 *Space Science Reviews* **141** URL <http://dx.doi.org/10.1007/s11214-007-9294-z>
- [9] Fraser-Smith A C, Bernardi A, McGill P R, Ladd M E, Helliwell R A and Villard O G 1990 *Geophysical Research Letters* **17** 1465–1468 ISSN 1944-8007 URL <http://dx.doi.org/10.1029/GL017i009p01465>
- [10] Yen H Y, Chen C H, Yeh Y H, Liu J Y, Lin C R and Tsai Y B 2004 *Earth Planets Space* **56** 39
- [11] Hayakawa M, Schekotov A, Potirakis S and Eftaxias K 2015 *Proc. Japan Acad. Ser.* **B91**

- [12] Fraser-Smith A C and Coates D B 1978 *Radio Science* **13** 661–668 ISSN 1944-799X URL <http://dx.doi.org/10.1029/RS013i004p00661>
- [13] Chapman S and Bartels J 1962 *Geomagnetism. 2 2* (Oxford: Clarendon Press)
- [14] Higbie J M, Corsini E and Budker D 2006 *Review of Scientific Instruments* **77** 113106 URL <http://scitation.aip.org/content/aip/journal/rsi/77/11/10.1063/1.2370597>
- [15] Benediktsson J A, Palmason J A and Sveinsson J R 2005 *IEEE Transactions on Geoscience and Remote Sensing* **43** 480–491 ISSN 0196-2892
- [16] Kruse F A and Elvidge C D 2011 Identifying and mapping night lights using imaging spectrometry *Aerospace Conference, 2011 IEEE* pp 1–6 ISSN 1095-323X
- [17] Dobler G, Ghandehari M, Koonin S E and Sharma M S 2016 *Sensors* **16** ISSN 1424-8220 URL <http://www.mdpi.com/1424-8220/16/12/2047>
- [18] Dobler G, Ghandehari M, Koonin S E, Nazari R, Patrinos A, Sharma M S, Tafvizi A, Vo H T and Wurtele J S 2015 *Information Systems* **54** 115 – 126 ISSN 0306-4379 URL <http://www.sciencedirect.com/science/article/pii/S0306437915001167>
- [19] Pustelny S, Jackson Kimball D F, Pankow C, Ledbetter M P, Włodarczyk P, Wcisło P, Pospelov M, Smith J R, Read J, Gawlik W and Budker D 2013 *Annalen der Physik* **525** 659–670 ISSN 1521-3889 URL <http://dx.doi.org/10.1002/andp.201300061>
- [20] Korver N 2003 Adequacy of the universal serial bus for real-time systems Tech. rep. University of Twente URL <http://doc.utwente.nl/56344/1/Korver03adequacy.pdf>
- [21] Torrence C and Compo G P 1998 *Bulletin of the American Meteorological Society* **79** 61–78
- [22] Farge M 1992 *Annual Review of Fluid Mechanics* **24** 395–458 (Preprint <http://dx.doi.org/10.1146/annurev.fl.24.010192.002143>) URL <http://dx.doi.org/10.1146/annurev.fl.24.010192.002143>
- [23] Podesta J J 2009 *Astrophysical Journal* **698** 986–999 (Preprint [0901.4940](http://arxiv.org/abs/0901.4940))
- [24] Bendat J S and Piersol A G 1990 *Random Data: Analysis and Measurement Procedures* 2nd ed (New York, NY, USA: John Wiley & Sons, Inc.) ISBN 0471040002
- [25] Singh Y P and Badruddin 2006 *Journal of Atmospheric and Solar-Terrestrial Physics* **68** 803–813
- [26] Connors M, Schofield I, Reiter K, Chi P J, Rowe K M and Russell C T 2016 *Earth, Planets and Space* **68** 1–21 ISSN 1880-5981 URL <http://dx.doi.org/10.1186/s40623-015-0354-4>